Frequency-Domain Method for Rotor Self-Noise Prediction

Q. Zhou* and P. F. Joseph†

University of Southampton, Highfield, Southampton, England SO17 1BJ, United Kingdom

A frequency-domain formulation is described for predicting the broadband self-noise radiation from an open rotor, or propeller, situated in a smooth, mean flow. It is assumed that the noise is predominantly due to the interaction between the hydrodynamic pressure associated with the turbulent boundary layer over the rotor blades and their trailing edges. Integration of the aerodynamic sources is performed over the actual blade surface rather than on the projected disk or nonthickness blade surface, as having being done in previous studies, thereby avoiding the commonly made assumption of flat plate geometry. The validation is performed of predictions of the measured broadband noise from an R212 propeller. Acceptable agreement between the measurement and predicted noise spectrum is obtained. The broadband self-noise directivity is also investigated, which is found to vary only slowly with azimuthal angle, with a main lobe in the direction of the propeller axis. The theory is used to undertake a parameter study of the broadband noise radiation from the propeller. Effects due to chord, blade number, and angle of attack are also discussed.

Nomenclature

$\bar{A}$	=	amplitude of an oscillation quantity A in frequency domain
$\hat{A}$	=	amplitude of an oscillation quantity A in frequency-wave number domain
$\tilde{A}$	=	nondimensional version of quantity A
c	=	airfoil chord length
c_u	=	convective velocity coefficient
c_0	=	speed of sound
D	=	directivity function, rotor diameter
f_p	=	position-transfer function of the wall pressure spectrum, defined by Eq. (11)
f_T, f_R, f_D	=	forces per unit area exerted by the rotor blades in y_1, r_0, and θ_0 directions
G	=	Green function in the time domain
$\bar{G}$	=	Green function in the frequency domain
H_l	=	transfer function of the lth mode between p and p_i
H_q	=	transfer function between p_t and p_i
H_s	=	transfer function between Δp_s and p_i
K	=	$\sqrt{[\mu_0^2 - (k_t/\beta_0)^2]}$
k	=	streamwise wave number and spanwise wave number, (k_s, k_t)
l	=	integer indicating the order of blade pasing frequency, 0, ±1, ±2, ±3, . . .
l_1	=	boundary-layer integral length scale in the streamwise direction
l_2	=	boundary-layer integral length scale in the spanwise direction
M	=	rotor forward flight Mach number, U/c_0
M_h	=	blade tip Mach number
M_0	=	airfoil or blade section Mach number, U_0/c_0
m	=	$N_b l$
N_b	=	blade number
n	=	unit normal vector pointing inward from the blade surface, (n_1, n_r, n_θ)
p	=	radiated acoustic pressure
p_i	=	incident pressure due to boundary-layer turbulence
p_{ref}	=	reference pressure, 2×10^{-5} Pa
p_s	=	scattered pressure due to trailing edge
p_t	=	pressure on airfoil surface or blade surface, $p_i + p_s$
R	=	mean-flow corrected distance defined by Eq. (20)
R_d	=	observation distance, $\sqrt{(x_1^2 + r^2)}$
R_s	=	$\sqrt{(x_1^2 + \beta^2 r^2)}$
r	=	radial coordinate of observation point in cylindrical coordinate system
r_0	=	radial coordinate of source point in cylindrical coordinate system
S_{pp}	=	sound pressure spectral density
S_{qq}	=	frequency-wave number spectral density of wall pressure, defined by Eq. (5)
S_0	=	boundary-layer frequency spectrum of point wall pressure
S_1	=	wave number spectra in streamwise direction
S_2	=	wave number spectra in spanwise direction
t	=	time associated with arrival of sound wave at observation point
U	=	rotor forward flight velocity
U_c	=	convective velocity
U_0	=	airfoil velocity or blade section velocity at a rotor radius
x	=	coordinates associated with observation point; (x_1, r, θ') for cylindrical coordinates and (x_1, x_2, x_3) for rectangular coordinate system
y	=	coordinates associated with source point; (y_1, r_0, θ_0') for cylindrical coordinates and (y_1, y_2, y_3) for rectangular coordinate system
y^b	=	blade-fixed coordinates associated with source point; (y_1, r_0, θ_0) for cylindrical coordinates and (y_1^b, y_2^b, y_3^b) for rectangular coordinate system
y^b_{TE}	=	coordinate value of y^b at the trailing edge
y_0	=	reference point for position-transfer function on the airfoil trailing edge or on blade trailing edge
α	=	attack angle at a blade radius section, $\beta_P - \beta_H$
β, β_0	=	$\sqrt{(1 - M^2)}$ and $\sqrt{(1 - M_0^2)}$, respectively
β_H	=	inflow angle at a blade radius section
β_P	=	geometric pitch angle of blade
Δp_s	=	scattered pressure jump across a flat plate airfoil
δ	=	Dirac delta function; boundary-layer thickness

*Ph.D. Student, Institute of Sound and Vibration Research; currently Assistant Professor, Ship Science Department, 717 Jia Fang Road, Wuhan 430033, People's Republic of China.

†Senior Lecturer, Institute of Sound and Vibration Research.

δ^*	=	boundary-layer displacement thickness
η	=	curvilinear coordinate system on blade surface, in streamwise direction and in spanwise direction, respectively, (η_s, η_t)
θ	=	azimuthal angle of observation point in blade-fixed cylindrical coordinate system
θ_0	=	azimuthal angle of source point in blade-fixed cylindrical coordinate system
κ, κ_0	=	ω/c_0 and ω_0/c_0, respectively
μ, μ_0	=	κ/β^2 and κ_0/β_0^2, respectively
ν	=	flow region
ρ_0	=	density of steady background flow
σ_1	=	reduced frequency, $k_s c/2$
τ	=	time associated with emission of sound wave at source point
Ψ	=	azimuthal angle measured from x_1 axis, $\cos^{-1}(x_1/R_d)$
ψ	=	$\cos^{-1}(x_1/R_s)$
Ω	=	angular speed of rotor
ω	=	observation frequency in forward-flight coordinate system
ω_0	=	source frequency in blade-fixed coordinate system

I. Introduction

THE noise produced by rotating blades may be formulated either in the time domain or the frequency domain. Lowson[1] has obtained a general expression in the time domain for the sound field due to a point force in arbitrary motion. His expression provides clear insight into the mechanism of sound generation in terms of the time rate of change of the force distribution acting on the fluid and the acceleration of the system in which the force is acting. An alternative approach is taken by Ffowcs Williams and Hawkings,[2] who generalize Lighthill's acoustic analogy approach to include surfaces in arbitrary motion. Lowson's formulation and Ffowcs Williams and Hawkings's equations are quite general. However, both are time-domain formulations, which involve convolution-type integrals to be evaluated. Farassat[3] has developed a practical time-domain method for the calculation of rotating blade noise. The time-domain method is readily applied to arbitrary blade geometry but requires source strength time histories to be known, as well as requiring numerical differentiation and calculations of the retarded blade positions to be performed.

Transformation of the governing equation to the frequency domain eliminates the need for computing retarded blade locations and provides clearer insight into the influence on noise of blade geometry. Hanson[4,5] has proposed a frequency-domain formulation for propellers in flight via a helicoidal surface representation of the blades corresponding to the path followed by a point on the blade during flight. Hanson's integration is evaluated on the helicoidal surface of the blade midchord, and hence, a thin-blade approximation has to be made. However, as pointed out by Peake and Crighton,[6] integration over the mean plane is inappropriate when the airfoil thickness is comparable with the Doppler-shifted wavelength. In particular, great care must be exercised when considering Mach radiation for which the effective Doppler frequency is infinite. Although Hanson's helicoidal surface theory,[4] which was used for making tone noise prediction, may in principle be extended to broadband noise predictions, the source integration is confined to the nonthickness blade surface. This leads to potentially significant phase errors at high frequency at radiation angles close to the propeller axis.[4] However, the broadband directivity predictions presented later indicate strong radiation in these directions. Therefore, a new frequency-domain formulation without the use of the thin-blade approximation is necessary for more making accurate rotor noise prediction.

Frequency-domain approaches have recently been extended to nonaxially symmetric sound fields based on the unsteady (once per revolution) loading experienced by the propeller blades when the propeller axis is at nonzero angle of attack to the freestream flow direction.[7,8] A simplifying assumption made in this paper is that the uniform flow stream is along the propeller axis.

An important application of the new frequency-domain formulation is that it can be easily extended for making broadband noise predictions. Broadband noise radiated from a propeller or rotor can be classified into either in-flow noise or self-noise (for example, Brooks[9]). In-flow noise is due to turbulent flow impinging on the rotating blades. Some early work on broadband inflow noise from rotors is by Paterson and Amiet,[10] Amiet et al.,[11] and Homicz and George.[12] Self-noise is due to blade self-generated turbulence interacting with the blade trailing edge. Howe[13] has presented a review of the literature on the theory of airfoil self-noise generation. A recent study that includes the contribution of oblique pressure gusts to airfoil self-noise radiation is given by Roger and Moreau.[14] However, for rotor self-noise prediction, only semi-empirical models (for example, Brooks and Burley[15]) have been developed. A generalized theory for the prediction of self-noise radiation from rotors is presented later.

This paper describes a frequency-domain approach for the prediction of far-field broadband noise radiated from an open rotor or propeller. The relationship between the spectrum of unsteady surface pressure and the radiated far-field spectrum is clearly established. The approach has also been used to calculate the tonal noise when the surface pressure is taken as the steady force due to the lift and drag acting on the blade.[16] The approach has particular application to rotor broadband self-noise; although with only small modifications, it is readily extended to include broadband in-flow noise. The generalized formulation presented here allows for the integration of the steady and unsteady forces over the real blade surfaces, and hence, no thin-airfoil approximation is made, unlike in much of the earlier work, where the sources are assumed to be distributed over a nonthickness blade surface or on a plane of rotation.

The unsteady blade loading, which constitutes the aerodynamic sound sources, is predicted by combining isolated thin-airfoil theory,[16] the Corcos model of the turbulence wave number pressure spectrum,[17] the measured boundary-layer frequency spectrum obtained by Chou and George,[18] and the boundary thickness measurements made by Brooks et al.[19] Strip theory is used to extend the isolated airfoil theory for aerodynamic noise source to a rotating blade, which assumes that the boundary-layer turbulence at a particular spanwise position is the same as an airfoil of infinite span with prismatic cross section with the same incoming mean velocity and angle of attack.
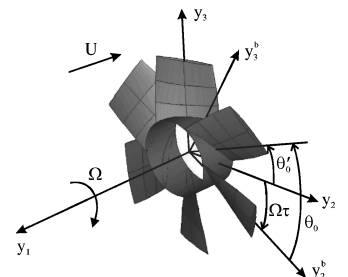
II. Coordinate Systems

The analysis presented here is formulated in a moving reference frame (airplane-fixed coordinates), which moves with constant velocity $\boldsymbol{U} = (U, 0, 0)$, as shown in Fig. 1. In the moving reference frame, the coordinates of the observation point and source point in a cylindrical coordinate system are denoted by $\boldsymbol{x} = (x_1, r, \theta')$ and $\boldsymbol{y} = (y_1, r_0, \theta_0')$, respectively. The relationships between the rectangular coordinate system and the cylindrical coordinate systems are
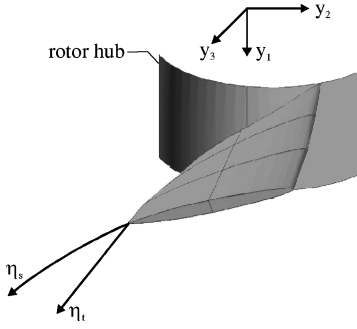
$$x_1 = x_1, \qquad x_2 = r\cos\theta', \qquad x_3 = r\sin\theta' \qquad (1)$$

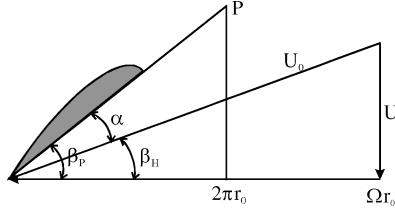$$y_1 = y_1, \qquad y_2 = r_0\cos\theta_0', \qquad y_3 = r_0\sin\theta_0' \qquad (2)$$

In the blade-fixed coordinates, the observation point and the source point are denoted by $\boldsymbol{x}^b = (x_1, r, \theta)$ and $\boldsymbol{y}^b = (y_1, r_0, \theta_0)$,

Fig. 1 Relation between moving coordinate system $\boldsymbol{y} = (y_1, r_0, \theta_0')$ and blade-fixed coordinate system $\boldsymbol{y}^b = (y_1, r_0, \theta_0)$.

Fig. 2 Blade curvilinear coordinate system (η_s, η_t) and associated wave number (k_s, k_t).

Fig. 3 Geometric pitch triangle and hydrodynamic velocity triangle, pitch angle β_P, hydrodynamic angle β_H, and attack angle α, where arrow indicates direction of fluid velocity.

respectively. The transformations between the moving coordinate system and the blade-fixed coordinate system are $\theta' = \theta - \Omega\tau$ and $\theta'_0 = \theta_0 - \Omega\tau$, where τ is the emission time and Ω is the angular velocity of the blade rotating in the opposite direction of θ'_0, as shown in Fig. 1.

In addition to the rectangular coordinate system $\mathbf{y} = (y_1, y_2, y_3)$ used in this paper, we also make use of the curvilinear coordinate system $\boldsymbol{\eta} = (\eta_s, \eta_t)$ to express the surface pressure distribution, as shown in Fig. 2. Here $\eta_s = \eta_s(\mathbf{y}^b)$ is the streamwise arc length with the origin located at the trailing edge and $\eta_t = \eta_t(\mathbf{y}^b)$ is the spanwise arc length normal to η_s on the suction-side or pressure-side surface. Correspondingly, we use k_s and k_t to denote the streamwise wave number and the spanwise wave number, respectively.

If we use a cylinder of radius r_0 cut through the propeller blade with cylinder axis coincident to the propeller axis, the blade section profile will closely fit on the cylinder surface. Unwrapping the cylinder surface onto a flat plane forms a right-angled triangle, as shown in Fig. 3.

The adjacent side of the triangle is the circumference $2\pi r_0$ of the end of the cylinder circular. The opposite side is the advanced distance (pitch distance) P of a point along the helicoidal chord line when the point rotates with a full circular angle. The hypotenuse of the triangle forms part of the blade section chord line as shown in Fig. 3. The angle formed between the adjacent side and the hypotenuse is referred to as the geometric pitch angle β_P. Figure 3 also shows the velocity triangle formed from the propeller forward flight velocity U, the blade section rotational velocity Ωr_0, and the resultant inflow velocity given by $U_0 = \sqrt{[U^2 + (\Omega r_0)^2]}$. This velocity triangle gives the in-flow angle as $\beta_H = \tan^{-1}(U/\Omega r_0)$ and, hence, the attack angle of the blade section as $\alpha = \beta_P - \beta_H$.

III. Spectra of Incident Aerodynamic Pressure Field

To make self-noise predictions, it is convenient to use as input data the boundary-layer pressures on the blade surface measured sufficiently far from the trailing edge such that its effects on the boundary layer are negligible. This distance is approximately one hydrodynamic wavelength from the trailing edge, as demonstrated by, for example, Ffowcs Williams and Hall[20] and Brooks and Hodgson.[21] We define the unsteady incident pressure p_i as that developed beneath the turbulent boundary layer on an infinite wall in the absence of the trailing edge and the pressure subsequently scattered from the trailing edge as the scattered pressure p_s. The scattered pressure may be deduced from p_i by solving the wave equation and imposing on the solution the boundary conditions of zero normal particle velocity on the airfoil surface and zero pressure difference at

the airfoil trailing edge (Kutta condition). These two pressures add to form the total airfoil surface pressure $p_t = p_i + p_s$ with trailing edge present. Once the relationship between p_i and p_s is established, the problem of broadband self-noise prediction is completely determined in principle from the incident pressure spectrum.

The unsteady wall pressure $p_i(\mathbf{y}, \tau)$ of the turbulence incident upon the trailing edge can be written in terms of its wave number-frequency components $\hat{p}_i(\mathbf{k}, \omega_0)$ by the Fourier transform relation

$$\hat{p}_i(\mathbf{k}, \omega_0) = \frac{1}{(2\pi)^3} \int_{-\infty}^{\infty} \int_{-\infty}^{\infty} \int_{-\infty}^{\infty} p_i(\mathbf{y}, \tau)$$

$$\times \exp[-i(k_s\eta_s + k_t\eta_t - \omega_0\tau)] \, d\eta_s \, d\eta_t \, d\tau \qquad (3)$$

where $\mathbf{k} = (k_s, k_t)$, $\boldsymbol{\eta} = (\eta_s, \eta_t)$, and ω_0 is the angular frequency. For broadband problems, it is useful to work with pressure wave number-frequency spectral densities. For simplicity, we assume here that the turbulent pressure field is spatially homogeneous and stationary with respect to time, that is, the space–time correlations of the boundary-layer pressure field are dependent only on the separation distance and temporal interval. Under this assumption, the wall-pressure frequency-wave number spectral density $S_{qq}(\mathbf{k}, \omega_0)$ are related to the Fourier components of wall pressure $\hat{p}_i(\mathbf{k}, \omega_0)$ by

$$E[\hat{p}_i^*(k_s, k_t, \omega_0)\hat{p}_i(k'_s, k'_t, \omega'_0)]$$

$$= \delta(k'_s - k_s)\delta(k'_t - k_t)\delta(\omega'_0 - \omega_0)S_{qq}(k_s, k_t, \omega_0) \qquad (4)$$

where $S_{qq}(k_s, k_t, \omega_0)$ is the wave number-frequency spectral density of the turbulence wall pressure, the asterisk superscript denotes complex conjugation, $E[\cdots]$ denotes the expected value, and δ is the Dirac delta function.

The surface pressure boundary-layer spectrum is dominated by its convective region[22] in which eddies convect at speeds slower than the speed of sound. The wave number spectrum of this region has been investigated by Corcos,[17] who proposes the following separable form for the frequency-wave number spectrum:

$$S_{qq}(\mathbf{k}, \omega_0) = S_0(\omega_0)S_1(k_s)S_2(k_t) \qquad (5)$$

where S_0 is the boundary-layer frequency spectrum, S_1 and S_2 are the normalized wave number spectra in the streamwise and transverse directions, respectively,

$$S_1(k_s) = (l_1/\pi)\left\{1/\left[1 + l_1^2(\omega_0/U_c - k_s)^2\right]\right\} \qquad (6)$$

$$S_2(k_t) = (l_2/\pi)\left\{1/\left[1 + l_2^2 k_t^2\right]\right\} \qquad (7)$$

where l_1 and l_2 are the boundary layer integral length scales in these directions, respectively. If the convection speed U_c is assumed to be constant, data obtained from experiments performed by Brooks[21] gives $l_1 = U_c/(0.11\omega_0)$ and $l_2 = U_c/(0.6\omega_0)$.

The pressure frequency spectrum $S_0(\omega_0)$ in Eq. (5) is predicted here using empirical expressions obtained by Chou and George[18] for the surface pressure spectrum using experimental spectral data from airfoils obtained by Yu and Joshi[23] and Brooks and Hodgson.[24] Two expressions are proposed encompassing the low and high range of frequencies. In the low-frequency range, $\tilde{\omega}_0 < 0.06$, the pressure frequency spectrum is of the form

$$\tilde{S}_0(\tilde{\omega}_0) = \frac{1.732 \times 10^{-3}\tilde{\omega}_0}{\left(1 - 5.489\tilde{\omega}_0 + 36.74\tilde{\omega}_0^2 + 0.1505\tilde{\omega}_0^5\right)} \qquad (8)$$

whereas in the higher-frequency range, $0.06 \leq \tilde{\omega}_0 \leq 20$, the frequency spectrum is given by

$$\tilde{S}_0(\tilde{\omega}_0) =$$

$$\frac{1.4216 \times 10^{-3}\tilde{\omega}_0}{\left(0.3261 + 4.1837\tilde{\omega}_0 + 22.818\tilde{\omega}_0^2 + 0.0013\tilde{\omega}_0^3 + 0.0028\tilde{\omega}_0^5\right)} \qquad (9)$$

where $\tilde{S}_0(\tilde{\omega}_0) = S_0(\omega_0)(U_0/\delta^*)/(0.5\rho_0 U_0^2)^2$, $\tilde{\omega}_0$ is the nondimensional frequency defined by $\tilde{\omega}_0 = \omega_0\delta^*/U_0$ (Strouhal number with respect to δ^*), where δ^* is the displacement thickness of the turbulent boundary layer, and U_0 is the freestream mean flow velocity external to the boundary layer. The calculation of the displacement thickness δ^* for arbitrary chord, angle of attack, and flow speed can be found from empirical formula based on measured data for a NACA0012 airfoil data.[19]

A simplification of the boundary-layer turbulence description may be obtained by making the assumption that turbulence convects as a frozen pattern at the convection velocity U_c. For frozen boundary-layer turbulence, the incident wall pressure spectrum may be written as[16]

$$\hat{S}_{qq}(\mathbf{k}) = \int_{-\infty}^{\infty} S_{qq}(\mathbf{k}, \omega_0)\, \mathrm{d}\omega_0 = U_c S_0(k_s U_c) S_2(k_t) \qquad (10)$$

Corcos assumes that a stationary and homogeneous pressure field is developed in the fully turbulent boundary layer without mean-pressure gradients over the flat plate, whereby the statistical properties of the pressure field change very little in the streamwise direction over a length comparable either to a transducer size or to a typical turbulence scale. The characteristics of the boundary-layer turbulence on a rotor blade differs from that on a flat plate in three important respects: 1) Boundary-layer thickness varies along the streamwise direction. 2) Local incoming velocity U_0 is nonuniform due to potential flow effects. 3) There is a pressure gradient in the streamwise direction within the boundary layer. We assume here that the boundary-layer thickness, the incoming velocity, and the pressure gradient are uniform over a small facet of the airfoil surface so that the Corcos pressure spectrum remain locally valid. We further assume that an airfoil with the same local inflow velocity $U_0(\mathbf{y})$ and boundary layer thickness $\delta^*(\mathbf{y})$ develops the same pressure frequency-wave number spectrum as a flat plate under the same conditions. Corcos's model of pressure spectrum will, therefore, be extended to a realistic airfoil by applying it locally to a small region on the airfoil surface, which is small compared with an acoustic and hydrodynamic wavelength. Although the Corcos model may not apply in some conditions, such as nearly detached flows at some spanwise locations (see Ref. 25), the Corcos model is used in this paper due to a lack of more precise input data.

A single frequency-wave number component of the incident surface pressure field can be written as $p_i(\mathbf{y}, \tau) = \bar{p}_i(\mathbf{y}, \omega_0)e^{-i\omega_0\tau}$, where $\bar{p}_i(\mathbf{y}, \omega_0) = \hat{p}_i(\mathbf{k}, \omega_0)e^{i\mathbf{k}\cdot\eta}$. However, as pointed out by Amiet,[26] use of this expression suggests that the pressure field appears suddenly at the airfoil leading edge, which is nonphysical. A more physically realistic representation of the incident pressure would be one in which the pressure gradually increases from zero at the leading edge, to reach its maximum value at the trailing edge, and which was identically zero farther downstream. Accordingly, Amiet[26] introduces an exponential decay function $f_p = e^{-\varepsilon|k_s\eta_s|}$, which multiplies $p_i(\mathbf{y}, \tau)$ to give the desired behavior, where ε is a decay factor that is chosen arbitrarily and generally differs at each frequency. Here, we define another function f_p in a manner that is consistent with the surface pressure spectra predictions made locally on the airfoil surface, which has the requisite behavior of Amiet's decay function. Equations (8) and (9) suggest that the wall pressure spectrum is a function of position $\mathbf{y}$ on the airfoil surface due to boundary-layer growth. A less arbitrary choice of decay function is the position-dependent function defined in terms of

$$f_p(\mathbf{y}, \mathbf{k}, \omega_0) = \sqrt{\frac{S_{qq}(\mathbf{y}, \mathbf{k}, \omega_0)}{S_{qq}(\mathbf{y}_0, \mathbf{k}, \omega_0)}} \qquad (11)$$

where $\mathbf{y}_0$ is an arbitrary reference point at the airfoil trailing edge. Note that unlike Amiet's decay factor, Eq. (11) is identically zero at the leading edge, reaching a maximum value at the trailing edge for all frequencies and wave number components. A single spectral component of the incident surface pressure field can, therefore, be written as $p_i(\mathbf{y}, \tau) = f_p(\mathbf{y}, \mathbf{k}, \omega_0)\bar{p}_i(\mathbf{y}, \omega_0)e^{-i\omega_0\tau}$.

IV. Unsteady Blade Surface Pressure Estimation

The relationship between a single wave number component of pressure p_i normally incident upon the trailing edge from one side of a flat plate airfoil and the pressure jump $\Delta\bar{p}_s$ due to this pressure being scattered from the trailing edge for a two-dimensional flat plate airfoil was derived by Amiet.[27] This was achieved by solving the linear Helmholtz equation subject to the imposition of the Kutta condition at the trailing edge and the no-flow condition on the blade surface. Amiet's two-dimensional solution has been extended to include wave number components of boundary-layer pressure arriving at oblique angles to the trailing edge.[16] The result has been used to define a transfer function H_s that relates the pressure jump $\Delta\bar{p}_s$ across the flat plate airfoil to the pressure $\bar{p}_i$ incident upon the trailing edge from one side:

$$\Delta\bar{p}_s(\mathbf{y}, \omega_0) = H_s(\mathbf{y}, \mathbf{k}, \omega_0)\bar{p}_i(\mathbf{y}, \omega_0) \qquad (12)$$

where H_s is given by

$$H_s(\mathbf{y}, \mathbf{k}, \omega_0) = \mathrm{erf}\left(\sqrt{i(K + \mu_0 M_0 + k_s)\eta_s}\right) - 1 \qquad (13)$$

where $K = \sqrt{[\mu_0^2 - (k_t/\beta_0)^2]}$, $\mu_0 = \kappa_0/\beta_0^2$, $\kappa_0 = \omega_0/c_0$, is the acoustic wave number related to the source frequency ω_0, c_0 is the speed of sound, and $M_0 = U_0/c_0$ is the Mach number related to the blade section velocity, $\beta_0 = \sqrt{(1 - M_0^2)}$. Equation (12) is consistent with the solution formulated by Amiet[27] when μ_0 and k_s are set to be negative (note that Amiet uses $e^{i\omega\tau}$) and k_t is equal to zero and reduces to the solution given by Howe[28] for $M_0 = 0$.

Equations (12) and (13) relate to the pressure jump for a flat plate airfoil. For more realistic airfoil geometries, numerical methods such as the boundary element method may be used to obtain more accurate solutions but are prohibitive for broadband calculations because the computation time required in the calculation of H_s at each frequency and wave number, which involves a spectrum of wave numbers and frequencies, is currently excessive. However, the use of flat plate theory is likely to be a reasonable approximation for trailing-edge noise calculations because the scattered pressure is only significant close to the trailing edge[20,21] where the airfoil is thinnest and most closely approximates a flat plate, assuming that no boundary-layer separation occurs. The effect of the airfoil geometry on the aerodynamic response function H_s is, therefore, ignored, although the effects of airfoil geometry on sound radiation, taking into account retarded time effects, are included in the formulation by integrating over the actual blade surface. We further make the approximation of high-reduced frequency $\sigma_1 = \kappa_c b$ where b is airfoil semichord, so that the effects of secondary scattering by the leading edge may be ignored.[25]

The transfer function defined in Eq. (13) relates to the pressure jump across the flat plate.[27,28] Howe[28] has shown, from a low-Mach-number approximation to the trailing-edge problem, that the scattered pressures on the surface of each side of the flat plate are identical in magnitude and equal to $\frac{1}{2}|\Delta\bar{p}_s|$, whereas the phase of the scattered pressures differs by 180 deg. When the position-dependent function $f_p(\mathbf{y}, \mathbf{k}, \omega)$ is taken into account in the definition of the incident pressure p_i, the total pressure p_t distributed over the surface of a real airfoil due to interaction with the trailing edge by a single frequency, single wave number, surface pressure component, $p_i(\mathbf{y}, \tau) = \bar{p}_i(\mathbf{y}, \omega_0)e^{-i\omega_0\tau}$, incident on one side of the airfoil may, therefore, be approximated by

$$p_t(\mathbf{y}, \tau) = p_i(\mathbf{y}, \tau) + p_s(\mathbf{y}, \tau) = H_q(\mathbf{y}, \mathbf{k}, \omega_0)\hat{p}_i(\mathbf{k}, \omega_0)e^{i(\mathbf{k}\cdot\eta - \omega_0\tau)}$$
$$(14)$$

where H_q is the transfer function between the surface pressure at any point on the airfoil surface $\eta = (\eta_s, \eta_t)$ and the incident pressure at the reference point $\mathbf{y}_0$ along the trailing edge, of the form

$$H_q(\mathbf{y}, \mathbf{k}, \omega_0) =$$

$$\begin{cases} f_p(\mathbf{y}, \mathbf{k}, \omega_0) + \frac{1}{2}H_s(\mathbf{y}, \mathbf{k}, \omega_0), & \mathbf{y} \text{ on the turbulence side} \\ -\frac{1}{2}H_s(\mathbf{y}, \mathbf{k}, \omega_0), & \mathbf{y} \text{ not on the turbulence side} \end{cases}$$
$$(15)$$

The application of Eq. (14) to a rotating blade requires the assumption that the blade section develops the same surface pressure distribution as an airfoil with the same local incoming velocity U_0, the same angle of attack α, and the same section geometry. For a rotating blade, the turbulence wall pressure $p_t(\boldsymbol{y}, \tau)$ is measured in the blade-fixed coordinate system, which we now denote by $p_t(\boldsymbol{y}^b, \tau)$. This surface pressure varies along blade spanwise direction. The variation is accommodated in the position transfer function, which we now indicate by $f_p(\boldsymbol{y}^b, \boldsymbol{k}, \omega_0)$. Note that $f_p(\boldsymbol{y}^b, \boldsymbol{k}, \omega_0)$ varies in the streamwise direction as well as the blade spanwise direction because the incoming velocity U_0 and the angle of attack α vary with the rotor radius r_0. For an airfoil of uniform profile, $f_p(\boldsymbol{y}, \boldsymbol{k}, \omega_0) = 1$ along the airfoil trailing edge. However, for a rotating blade, $f_p(\boldsymbol{y}^b, \boldsymbol{k}, \omega_0) \neq 1$ along the blade trailing edge. To ensure that the Kutta conditions are satisfied at any radius of blade trailing edge, Eq. (15) must be reformulated as

$$
H_q\left(\boldsymbol{y}^b, \boldsymbol{k}, \omega_0\right) = \begin{cases} f_p\left(\boldsymbol{y}^b, \boldsymbol{k}, \omega_0\right) + \frac{1}{2} f_p\left(\boldsymbol{y}_{\text{TE}}^b, \boldsymbol{k}, \omega_0\right) H_s\left(\boldsymbol{y}^b, \boldsymbol{k}, \omega_0\right), & \boldsymbol{y}^b \text{ on the turbulence side} \\ -\frac{1}{2} f_p\left(\boldsymbol{y}_{\text{TE}}^b, \boldsymbol{k}, \omega_0\right) H_s\left(\boldsymbol{y}^b, \boldsymbol{k}, \omega_0\right), & \boldsymbol{y}^b \text{ not on the turbulence side} \end{cases} \quad (16)
$$

where $\boldsymbol{y}_{\text{TE}}^b$ is the position at the trailing edge in the coordinate system aligned with the blade and $\boldsymbol{\eta} = \{\eta_s, \eta_t\} = \{0, \eta_t\}$. Note that the quantities M_0, β_0, μ_0, and K in Eq. (16) take their local blade section values at radius r_0.

For the general case of a turbulent pressure field incident upon the trailing edge, which involves a continuum over all wave number and frequency components, Eq. (14) generalizes to

$$
p_t(\boldsymbol{y}^b, \tau) =
$$

$$
\int_{-\infty}^{\infty}\int_{-\infty}^{\infty}\int_{-\infty}^{\infty} H_q\left(\boldsymbol{y}^b, \boldsymbol{k}, \omega_0\right) \hat{p}_i(\boldsymbol{k}, \omega_0) e^{i(k\cdot\eta - \omega_0 \tau)} \, \mathrm{d}^2\boldsymbol{k} \, \mathrm{d}\omega_0 \quad (17)
$$

where $\hat{p}_i(\boldsymbol{k}, \omega_0)$ is given by Eq. (3). Note that $\hat{p}_i(\boldsymbol{k}, \omega_0)$ and its related spectrum $S_{qq}(\boldsymbol{k}, \omega_0)$ now take values at a reference point $\boldsymbol{y}_0$ along the trailing edge.

V. Radiation Transfer Function and Pressure Spectrum

Our derivation of the theory of broadband noise radiation from a rotor begins with Goldstein's version[29] of the acoustic analogy. This is the fundamental equation governing the generation of aerodynamic sound in the presence of solid boundaries and takes the form for a flow region $\nu(\tau)$ exterior to an impermeable closed surface $S(\tau)$

$$
p(\boldsymbol{x}, t) = \int_{-T}^{T}\iiint_{\nu(\tau)} \frac{\partial^2 G}{\partial y_i \partial y_j} T_{ij}'(\boldsymbol{y}, \tau) \, \mathrm{d}\boldsymbol{y} \, \mathrm{d}\tau
$$

$$
+ \int_{-T}^{T}\iint_{S(\tau)} \frac{\partial G}{\partial y_i} f_i \, \mathrm{d}S(\boldsymbol{y}) \, \mathrm{d}\tau + \int_{-T}^{T}\iint_{S(\tau)} \rho_0 V_n' \frac{\mathrm{D}_0 G}{\mathrm{D}\tau} \, \mathrm{d}S(\boldsymbol{y}) \, \mathrm{d}\tau
$$

$$
(18)
$$

where f_i is the ith component of the force per unit area exerted by the boundaries on the fluid, T_{ij}' is Lighthill's stress tensor for isentropic flow, V_n' is the normal velocity of blade surface $S(\tau)$, the superscript primes on T_{ij}' and V_n' indicate the quantities are measured in the Earth-fixed reference frame, t is the time associated with the arrival of sound wave at the observation point, and T is some large but finite interval of time. In Eq. (18), $G = G(\boldsymbol{x}, t; \boldsymbol{y}, \tau)$ is the Green function solution for the free-space wave equation relating to a medium with uniform mean flow. This moving-medium Green's function in an unbounded medium is given by (see Ref. 16)

$$
G(\boldsymbol{x}, t; \boldsymbol{y}, \tau) = (1/4\pi R)\delta\left\{\tau + \left(1/\beta^2 c_0\right)[R + M(y_1 - x_1)] - t\right\} \quad (19)
$$

where $\beta^2 = 1 - M^2$, $M = U/c_0$ is the Mach number of the mean flow, and R is the mean-flow corrected distance,

$$
R = \sqrt{(y_1 - x_1)^2 + \beta^2\left[r^2 + r_0^2 - 2rr_0\cos(\theta_0 - \Omega\tau - \theta')\right]} \quad (20)
$$

Volume displacement source and quadrupole source are only important at relative flow speeds close to the sound.[30,31] We shall, therefore, confine our attention to the sound radiation due to the unsteady blade forces exerted by the blade surface on the adjacent fluid due to turbulence interaction with the airfoil and its trailing edge. Thus, we are concerned only with the second term of Eq. (18). Substituting the Green function of Eq. (19) into the second term of Eq. (18) and performing Fourier transformation with respect to t, we obtain the radiated pressure due to a single blade surface S_i, of the form

$$
\bar{p}(\boldsymbol{x}, \omega) = \frac{1}{2\pi}\int_{-T}^{T}\iint_{S_i} f_j(\boldsymbol{y}, \tau)e^{i\omega\tau} \frac{\partial}{\partial y_j}\bar{G}(\boldsymbol{x}, \boldsymbol{y}) \, \mathrm{d}S(\boldsymbol{y}) \, \mathrm{d}\tau \quad (21)
$$

where ω is the observed frequency related to time t at the observation point $\boldsymbol{x}$ and $\bar{G}$ is the Fourier transform of Eq. (19) of the form

$$
\bar{G}(\boldsymbol{x}, \boldsymbol{y}, \omega) = (1/4\pi R)\exp\{i\mu[R + M(y_1 - x_1)]\} \quad (22)
$$

where $\mu = \kappa/\beta^2$ and $\kappa = \omega/c_0$ is acoustic wave number related to the observation frequency ω.

We now make the far-field approximations: $r_0, y_1 \ll R_s$, where $R_s = \sqrt{(x_1^2 + \beta^2 r^2)}$ is the flow-corrected distance from the origin of the blade-fixed reference system to the observation point. Substituting the derivatives $\partial/\partial y_i$ of Eq. (22) into Eq. (21) and ignoring second-order terms, one obtains

$$
\bar{p}(\boldsymbol{x}, \omega) = \frac{-i\mu}{8\pi^2}\frac{e^{i\mu R_s}}{R_s}\int_{-T}^{T}\iint_{S_i}\left\{-f_T(y, \tau)\left[\frac{(y_1 - x_1)}{R_s} + M\right]\right.
$$

$$
+ f_R(y, \tau)\beta^2\left[-\frac{r_0}{R_s} + \sin\psi\cos(\theta_0' - \theta')\right]
$$

$$
- f_D(y, \tau)\beta^2\sin\psi\sin(\theta_0' - \theta')\Bigg\} \times e^{i\omega\tau}\exp[i\mu M(y_1 - x_1)]
$$

$$
\times \exp\left\{-i\mu\left[y_1\cos\psi + \beta^2 r_0\sin\psi\cos(\theta_0' - \theta')\right]\right\} \mathrm{d}S(\boldsymbol{y}) \, \mathrm{d}\tau
$$

$$
(23)
$$

where $\cos\psi = x_1/R_s$, $\sin\psi = r/R_s$, and f_T, f_R, and f_D are the forces per unit area exerted by the rotor blades in the y_1, r_0, and θ_0 directions, respectively. Here, the usual far-field approximation is made whereby $1/R$ is replaced by $1/R_s$. The forces in Eq. (23) are related to the blade surface pressure of Eq. (17) by

$$
\begin{Bmatrix} f_T \\ f_R \\ f_D \end{Bmatrix} = -\begin{Bmatrix} n_1 \\ n_r \\ n_\theta \end{Bmatrix} p_t(\boldsymbol{y}^b, \tau) \quad (24)
$$

where $\boldsymbol{n} = \{n_1, n_r, n_\theta\}$ is the unit normal vector pointing inward from the blade surface. To enable the integration with respect to τ to be performed in Eq. (23), the following generating function[32] for the Bessel function $J_m(Z)$ of the first kind of order m,

$$
\exp(iZ\cos\theta) = \sum_{m=-\infty}^{\infty} J_m(Z)\exp[im(\theta + \pi/2)]
$$

is used. Substituting Eqs. (17) and (24) into Eq. (23), and performing the integration with respect to τ and ω_0 for N_b blades, gives Eq. (25) for the radiated pressure of the form

$$\bar{p}(\boldsymbol{x}, \omega) = \sum_{l=-\infty}^{\infty} \int_{-\infty}^{\infty} \int_{-\infty}^{\infty} H_l(\boldsymbol{x}, \boldsymbol{k}, \omega, \omega + N_b l\Omega)$$

$$\times \hat{p}_s(\boldsymbol{k}, \omega + N_b l\Omega) \, \mathrm{d}^2\boldsymbol{k} \tag{25}$$

Note that the effects on the radiated sound field of scattering between adjacent blades are ignored in this formulation. Here, H_l is the transfer function between the radiated acoustic pressure at $\boldsymbol{x}$ and the lth harmonic pressure component on the blade surface of frequency ω_0 with wave numbers k_s and k_t and is given by

$$H_l(\boldsymbol{x}, k_s, k_t, \omega, \omega_0) = \frac{i\mu N_b}{4\pi R_s} \exp[i\mu(R_s - Mx_1)]$$

$$\times \exp\left[im\left(\theta' - \frac{\pi}{2}\right)\right] \iint_{S_i} \left\{ -n_1\left[\frac{(y_1 - x_1)}{R_s} + M\right] \right.$$

$$\left. - n_r\beta^2\left[\frac{r_0}{R_s} - i\sin\psi\left(\frac{m}{Z} - \frac{J_{m+1}(Z)}{J_m(Z)}\right)\right] + n_\theta\frac{\beta^2 m}{\kappa r_0} \right\}$$

$$\times H_q(\boldsymbol{y}^b, \boldsymbol{k}, \omega_0) \times \exp(i\boldsymbol{k} \cdot \boldsymbol{\eta}) \exp[i\mu(M - \cos\psi)y_1]$$

$$\times \exp(-iN_b l\theta_0) J_m(Z) \, \mathrm{d}S(\boldsymbol{y}^b) \tag{26}$$

where $Z = \kappa r_0 \sin\psi$ and $m = N_b l$ is the circumferential mode number and $l = 0, \pm1, \pm2, \pm3, \cdots$. For a steady force distribution on the blade surface, l is the order of the blade-passing frequency. For an unsteady force distribution on the blade surface, the pressure at frequency ω is due to the blade surface pressure at the frequency, $\omega_0 = \omega + N_b l\Omega$, which is the observed frequency shifted by the blade-passing frequency, $N_b l\Omega$.

For broadband excitation, $\bar{p}$ may be regarded as a random process that is most suitably expressed as a power spectral density defined by

$$S_{pp}(\boldsymbol{x}, \omega')\delta(\omega' - \omega) = E[\bar{p}^*(\boldsymbol{x}, \omega')\bar{p}(\boldsymbol{x}, \omega)] \tag{27}$$

Inserting Eq. (25) into Eq. (27), making use of the statistical orthogonality relationship of Eq. (4), and integrating the result with respect to ω' gives the power spectrum of far-field pressure in the form

$$S_{pp}(\boldsymbol{x}, \omega) = \sum_{l=-\infty}^{\infty} \int_{-\infty}^{\infty} \int_{-\infty}^{\infty} |H_l(\boldsymbol{x}, \boldsymbol{k}, \omega, \omega + N_b l\Omega)|^2$$

$$\times S_{qq}(\boldsymbol{k}, \omega + N_b l\Omega) \, \mathrm{d}^2\boldsymbol{k} \tag{28}$$

When frozen turbulence is assumed, $l_1 \to \infty$ and $S_1(k_s) \to \delta(k_s - \omega_0/U_c)$, which in Eq. (28) leads to

$$S_{pp}(\boldsymbol{x}, \omega) = \sum_{l=-\infty}^{\infty} \int_{-\infty}^{\infty} |H_l(\boldsymbol{x}, \boldsymbol{k}, \omega, \omega + N_b l\Omega)|^2 S_0(|k_s|U_c)S_2(k_t) \, \mathrm{d}k_t \tag{29}$$

where $k_s = (\omega + m\Omega)/U_c$, $U_c = c_u U_0 = c_u\sqrt{[U^2 + (0.7\Omega r_t)^2]}$, c_u is convective velocity coefficient, which is typically in the range $c_u = 0.65 \sim 0.8$. Note that the reference point for the position-transfer function f_p is taken at trailing edge of 0.7 rotor disk radius r_t.

The derived results for far-field radiation are shown by the authors to reduce to the classical solution due to Gutin[33] for tonal noise when the flight speed is set to zero and the steady source integral is confined to the projected disk of the rotating blades.[16] Homicz and George[12] extended Gutin's results for application to broadband in-flow noise from circularly shaped unsteady sources. Although Homicz and George claim that the approach is formally applicable to arbitrarily shaped source distributions, the source integration on real blade surface corresponds to a more general case, which cannot

be obtained from a straightforward integration of the source distribution over a projected disk. This is because the source integration must be performed on the blade-fixed reference and the τ integration in Eq. (23) cannot be directly carried out as for the case of projected disk integration. Furthermore, the mean-flow effect has not been included in Homicz and George's formulations. On the other hand, a simplified analysis based on the approach by Paterson and Amiet[10] and avoiding Bessel functions calculations could be simpler and faster in a high-frequency approximation. However, care should be taken because the source frequencies ω_0 are shifted by all possible negative and positive blade-passing frequencies, $N_b l\Omega$, to give an observation frequency ω [see Eqs. (25) and (26)] and the source frequency ω_0 may take a low value for a given observation frequency ω.

VI. Comparison of Self Noise Predictions with Experimental Data

Predictions obtained from the just developed theory are now compared against the experimental results reported by Trebble.[34] Noise radiation measurements were made for a four-bladed Dowty Rotol R212 propeller (NACA 16 sections) in a 24-ft wind tunnel. The propeller was mounted in a 1.2-m-diam nacelle with a quiet electric motor that is capable of drive speeds up to 2000 rpm. Figure 4 shows the geometry of this four-bladed propeller. The main geometric parameters of the full-scale propeller may be found in Ref. 34. The propeller diameter is 3.66 m. Trebble's measurements were made at propeller rotational speeds n of 1000 rpm at stream speeds U of 30 m/s for blade-setting angles β_s equal to 15.1, 17.3, 20.1, 22.4, and 32.1 deg. The blade-setting angle β_s is defined as the twist angle at the 0.70 radius. The blade setting angles β_s are related to the pitch angle described in Sec. II by $\beta_P = \beta_T + \beta_S$, where β_T is the blade twist angle relative to that at the 0.70 radius station, which is the standard position for setting the blade angle.

A numerical scheme has been developed for the efficient computation of the mode transfer function H_l (Ref. 16). The blade surface is meshed into triangle elements with a maximum dimension of 8–10 times less than the acoustic wavelength. This allows analytic integration over each element facet, whose integrand involves the rapidly oscillating source terms in Eq. (26). Figure 5 shows the pressure-side mesh ($\beta_s = 20.1$ deg) used to perform the numerical integration of Eq. (29). The mesh shown in Fig. 5 with a maximum element dimension of 25 mm is valid for frequencies of less than 1300 Hz. In Fig. 5, 1298 triangle elements are meshed on pressure side of the blade surface.

The unsteady blade loading, which constitutes the aerodynamic sound sources, is predicted using Eqs. (5–10), (13), and (16). Figure 6 shows a comparison between the predicted sound pressure level (SPL) spectral density in the transverse plane, that is, 90 deg to the axis, 5.49 m from the axis (black broken line) and the measured noise spectrum (solid line). Also shown is the background noise spectrum (light broken line) to indicate the quality of the measured data. The calculations are taken at a rotational speed of $n = 1000$ rpm, a forward flight speed of $U = 30$ m/s, and a blade setting angle of $\beta_s = 20.1$ deg.
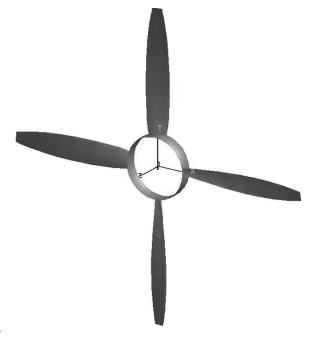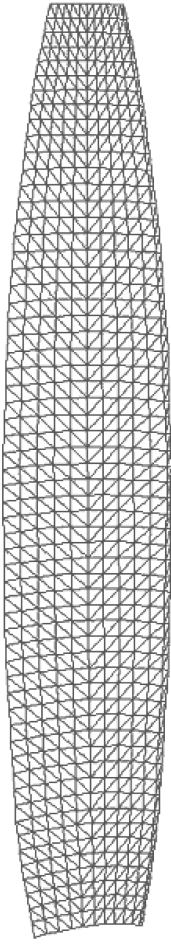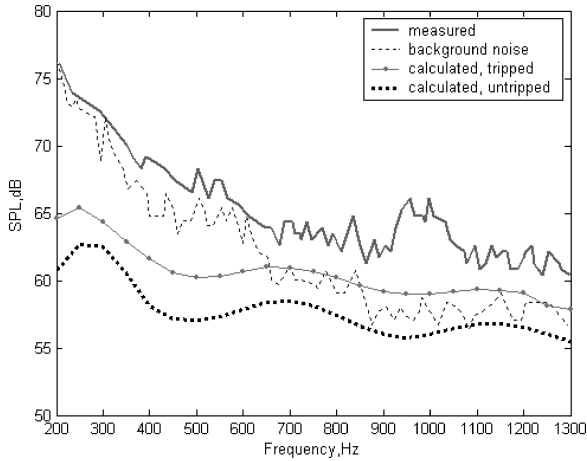

Fig. 4 Geometry of R212 propeller.

Fig. 5 Mesh for numerical calculation of R212 propeller, pressure side, $\beta_s = 20.1$ deg.

Fig. 6 Measured and predicted broadband self-noise from a R212 propeller at $R_d = 5.49$ m from the axis in plane of propeller, with rotational speed $n = 1000$ rpm, forward-flight speed $U = 30$ m/s, and blade-setting angle $\beta_s = 20.1$ deg.

The SPL is defined in decibels relative to $\boldsymbol{x} = (x_1, r, \theta')$ referred to $p_{\text{ref}} = 2 \times 10^{-5}$ Pa, based on an analysis bandwidth Δf of 11 Hz,

$$\text{SPL} = 10 \log_{10} \frac{4\pi \Delta f \, S_{pp}(\boldsymbol{x}, \omega)}{p_{\text{ref}}^2} \qquad (30)$$

where the factor 4π is included to account for 1) converting to a single sided ($0 < \omega < \infty$) spectrum and 2) converting from radian frequency to a 1-Hz bandwidth.

Agreement between predictions and measurements at frequencies above about 700 Hz are generally within 6 dB. Below 700 Hz, agreement is generally poorer. This may be due to the large background

noise levels at these low frequencies. However, spectral shape is closely predicted. The underestimated error over the whole frequency range may be due to the differences between the far-field assumption, on which Eq. (26) is based, and the measurement point, which may not be far enough from the propeller to justify the use of the far-field approximation. Additional error is introduced by making the frozen turbulence assumption, which is now known to underestimate the radiated noise.[16] The third possible reason for the error is that the surface pressure spectrum and the boundary-layer thickness, which determine the acoustic source on blade surface, are measured on a NACA 0012 airfoil rather than a NACA 16 series airfoil of which the R212 propeller is made. To assess the sensitivity of changes in the noise prediction to the source spectrum, the spectrum of the radiated pressure (dotted line) due to tripped boundary-layer turbulence is also plotted in Fig. 6. The tripped boundary-layer thickness used here is that measured by Brooks et al.[19] for a NACA 0012 airfoil. Boundary-layer turbulence tripping was achieved by placing random distributions of grit (nominal particle diameter of 0.29 mm with an application density of about 380 particles/cm^2) in strips from the leading edge to 20% chord. Figure 6 predicts a 3-dB increase in noise radiation due to tripping of the boundary-layer turbulence, suggesting that the radiated noise is sensitive to the details of the boundary-layer spectrum, for example, the location of the point of transition to turbulent flow. The fourth reason for the underestimated error may be due to a lack of knowledge of the wall-pressure loads because Corcos's model may not apply in some conditions, such as nearly detached flows at some spanwise locations (see Ref. 25). Furthermore, the noise due to the ingestion of turbulence may contribute to the radiated pressure at low frequencies. This contribution can be expected to be significant if the residual turbulence intensity in the oncoming flow is typically about 2%. Unfortunately Trebble[34] did not specify this value in his paper to allow quantification of this noise source. The formulation presented here can be used for both broadband and tone noise prediction. The tonal noise is predicted in very good agreement with measured data in Ref. 16 because in this case the acoustic source due to steady blade surface pressure can be predicted accurately.

VII. Directivity and Parameter Studies of Broadband Self-Noise

In this section, the theory developed in Sec. V is used to predict the directivity of the broadband noise radiated by the propeller. The directivity is defined by

$$D(\Psi, \omega) = 10 \log_{10} \left[\lim_{R_d \to \infty} R_d^2 \frac{4\pi S_{pp}(\boldsymbol{x}, \omega)}{p_{\text{ref}}^2} \right] \qquad (31)$$

where $\boldsymbol{x} = (R_d \cos \Psi, 0, R_d \sin \Psi)$ are the observation coordinates and the observer distance R_d is measured from the coordinate origin in the $x_2 = 0$ plane. For numerical calculation, we take $R_d = 100$ m. Figures 7 and 8 show the self-noise directivities in decibels of the R212 propeller in a 1-Hz bandwidth with center frequencies of 300 and 900 Hz, respectively.
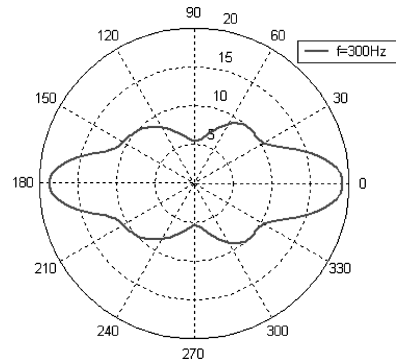
Fig. 7 Directivity $D(\Psi, \omega) -56.0$ at 300 Hz for axial flow velocity $U = 30$ m/s, blade rotational speed of $n = 1000$ rpm, $R_d = 100$ m, and $\beta_s = 17.3$ deg.
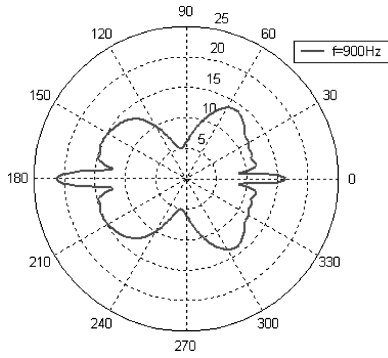
Fig. 8   Directivity $D(\Psi, \omega) - 52.0$ at 900 Hz for axial flow velocity $U = 30$ m/s, blade rotational speed of $n = 1000$ rpm, $R_d = 100$ m, and $\beta_s = 17.3$ deg.
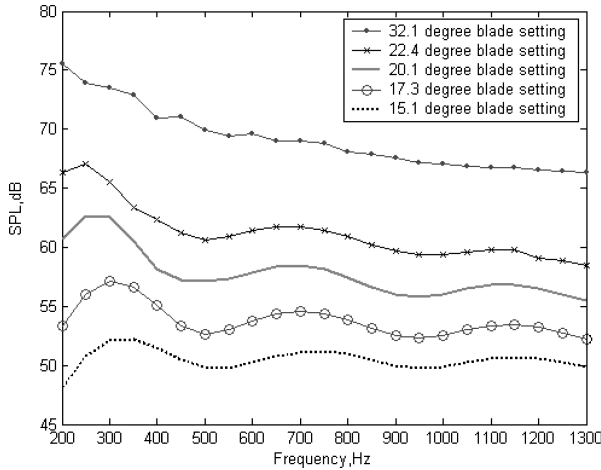

Fig. 9   Broadband self-noise at $R_d = 5.49$ m from propeller axis in plane of propeller, axial flow velocity $U = 30$ m/s, shaft rotational speed $n = 1000$ rpm, in a 11-Hz analysis bandwidth.

The self-noise radiation exhibits fairly weak directionality, with the variation of $D(\Psi, \omega)$ in Figs. 7 and 8 being less than about 15 dB over the entire range of polar angles. The main lobe of broadband self-noise directivity is in the direction of the propeller axis, whereas the main lobe of the tonal noise directivity due to a steady blade surface pressure distribution is normal to the propeller axial direction.[16] Mathematically, this is due to the following characteristics of the Bessel function in Eq. (26): $J_0(0) = 1$ and $J_m(0) = 0$ when $m \neq 0$. From Eq. (26), the source frequencies ω_0 are shifted by all possible blade-passing frequencies, $N_b l\Omega$, including the zero-order blade-passing frequency, that is, $l = 0$ in Eq. (26). For an unsteady source, the term $l = 0$ in Eq. (26) gives large contribution to the broadband noise in the propeller axial direction ($\psi = 0$) because $J_0(0) = 1$. However for a steady source, only the terms $l \neq 0$ produces noise at the blade-passing frequencies, and these terms make no contribution to the tonal noises in the propeller axial direction because $J_m(0) = 0$. The theory predicts a reduction in broadband noise near the plane of rotation. Experimental evidence for this prediction can be found in the classical work presented by Paterson and Amiet.[10] Here, the measured directivities near the plane of rotation are for broadband inflow noise, but is expected to have similar directivity characteristics as the broadband self-noise. Unfortunately Paterson and Amiet did not measure the rotor noise directivity in the axial direction.

The theory has also been used to undertake a parametric study of the broadband self-noise radiation from propellers with fan tip speed, number of blades, chord, and blade setting angle. Figure 9 shows a prediction of the pressure spectrum at $R_d = 5.49$ m from the R212 propeller axis in the plane of the propeller for various blade-setting angles. Increasing the blade-setting angle β_s is observed to increase self-noise radiation due to larger angle of attack and, hence,
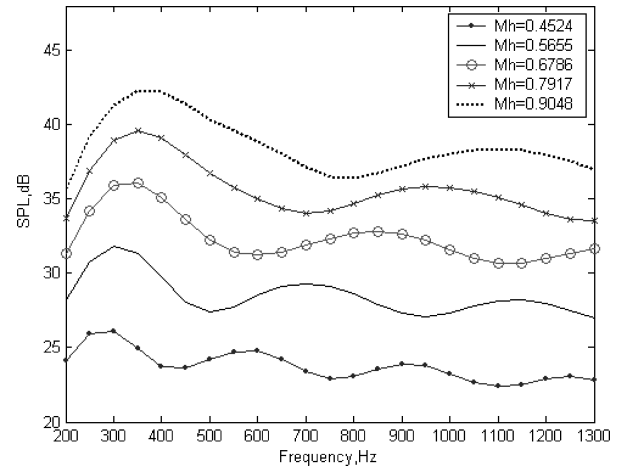

Fig. 10a   Broadband noise at $R_d = 100$ m for various blade tip Mach numbers M_h, in 11-Hz analysis bandwidth, $\beta_s = 17.3$ deg.
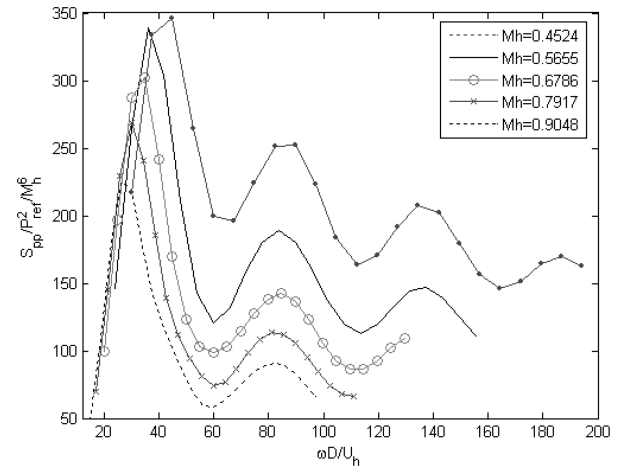

Fig. 10b   Predicted PSD to sixth power of blade tip Mach numbers M_h at $R_d = 100$ m, $\beta_s = 17.3$ deg.
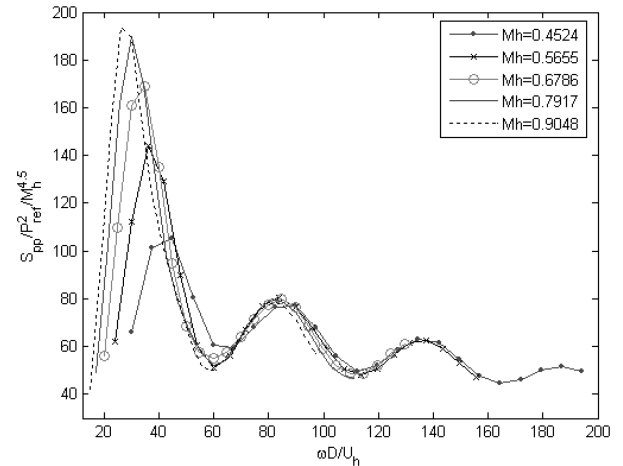

Fig. 10c   Predicted PSD to 4.5th power of blade tip Mach numbers M_h at $R_d = 100$ m, $\beta_s = 17.3$ deg.

larger boundary thickness and unsteady surface pressure. For each degree of increase in the blade-setting angle, the noise is predicted to increase by about 1.4 dB, except at the largest blade-setting angle of $\beta_s = 32.1$ deg, where flow separation is likely to have occurred.

Figure 10a shows the predicted dependence of the broadband noise frequency spectrum on the blade tip Mach number M_h for the R212 propeller. Note that in each case the angular speed Ω of the propeller and the forward-flight speed U are adjusted to keep

the tip section attack angle unchanged at $\alpha = 2$ deg. To deduce how the noise scales with blade tip speed, the result of Fig. 10a are replotted in a dimensionless form in Figs. 10b and 10c. In Fig. 10b, the ordinate is the dimensionless power spectrum density (PSD) S_{pp}/p_{ref}^2 divided by the blade tip Mach number M_h to the sixth power, whereas in Fig. 10c the ordinate is $S_{pp}/p_{ref}^2 M_h^{4.5}$. In Figs. 10b and 10c, abscissas are $\omega D/U_h$, where $U_h = M_h C_0$. The far-field PSD is found to scale very closely with the sixth power of the blade tip Mach number at low frequency ($\omega D/U_h < 30$) and to the 4.5th power at high frequency ($\omega D/U_h > 50$). Thickness noise and the noise due to the quadrupole source are ignored in the prediction of Fig. 10a. Note that these two sources may become important when the tip Mach number approaches unity.

We now consider self-noise radiation from two hypothetical propellers conceived specifically for the parametric study presented here. One has the same geometry as the R212 propeller already discussed but with the twist angle chosen such that a constant attack angle of 4 deg is obtained at an axial flow velocity of $U = 30$ m/s and a shaft rotational speed $n = 1000$ rpm. We refer to this geometry as the one-chord propeller. The blade number of this one-chord propeller is $N_b = 12$. The other propeller has the same geometry and the same constant attack angle of 4 deg as the one-chord propeller, but with a chord length of three times greater than that of the one-chord propeller. We refer to this as the three-chord propeller. However, this three-chord propeller has only 4 blades so that both the one-chord propeller and the three-chord propeller have approximately the same thrust area. Figures 11 and 12 show the geometry of these two propellers used in the calculation.

Because the two propellers have the same angle of attack, they should be able to provide approximately the same thrust. However, their noise levels are predicted to differ appreciably, as shown in Fig. 13, where the dashed line shows the SPL for the 12-blade one-chord propeller and the solid line denotes the SPL of the 4-blade
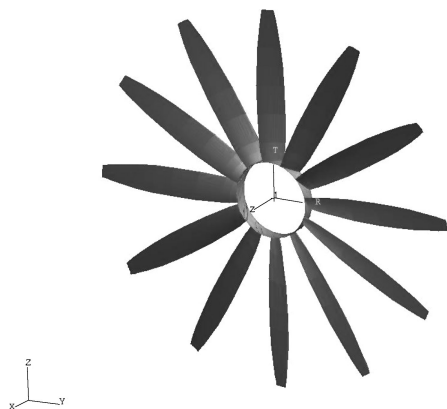

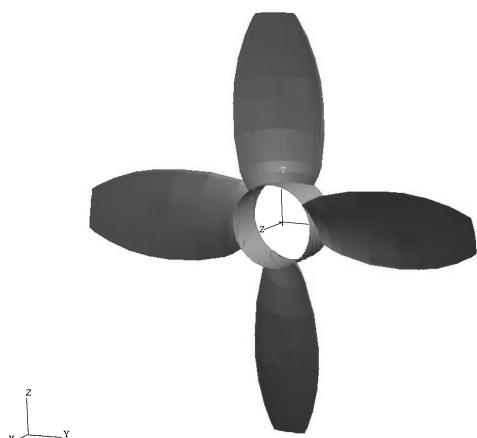**Fig. 11   Geometry of one-chord propeller.**

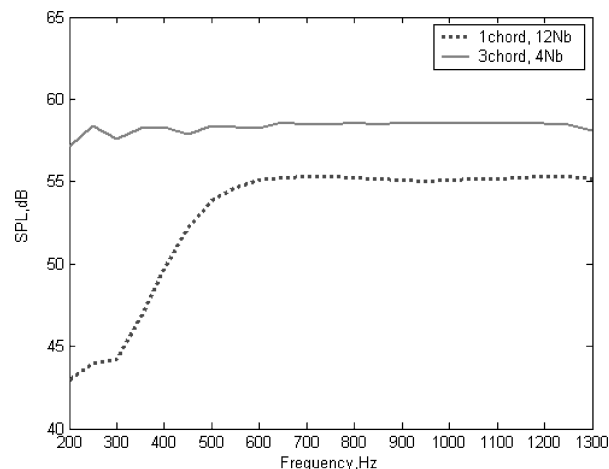**Fig. 12   Geometry of three-chord propeller.**

Fig. 13   Self-noise comparison between one-chord and three-chord propeller at $R_d = 5.49$ m from propeller axis in the plane of the propeller: axial flow velocity $U = 30$ m/s, shaft rotational speed $n = 1000$ rpm in a 11-Hz analysis bandwidth.
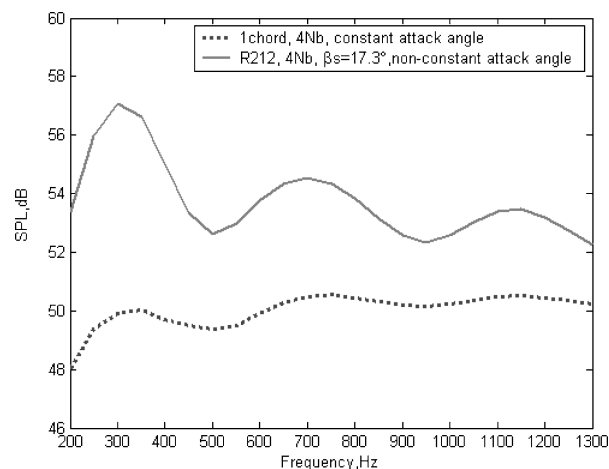

Fig. 14   Self-noise comparison between propellers of constant and non-constant angle of attack at $R_d = 5.49$ m from propeller axis in plane of the propeller: axial flow velocity $U = 30$ m/s, shaft rotational speed $n = 1000$ rpm in a 11-Hz analysis bandwidth.

three-chord propeller. The calculations are made at $R_d = 5.49$ m from the propeller axis in the plane of the propeller with an axial flow velocity of $U = 30$ m/s, a shaft rotational speed of $n = 1000$ rpm, and an 11-Hz analysis bandwidth. Figure 13 shows that the propeller with small chord and large blade number radiates the least noise, especially at low frequencies, where a difference in SPL of more than 10 dB is observed.

The main difference between the R212 propeller and the one-chord propeller is the blade twist angle. With the blade-setting angle equal to $\beta_s = 17.3$ deg, the attack angle of the R212 propeller varies from 10.2 deg at the blade root to 2.0 deg at the blade tip for an axial flow velocity of $U = 30$ m/s and a shaft rotational speed $n = 1000$ rpm. The one-chord propeller, however, has a constant attack angle of 4.0 deg. When it is noted that the blade tip section has a higher speed than the root section, and that the airfoil lift depends on both the attack angle and the airfoil velocity, these two propellers should deliver roughly the same thrust if the one-chord propeller has the same number of blades (equal to four) as the R212 propeller. Figure 14 shows a comparison between the self-noise due to this change of attack angle at an observation distance of $R_d = 5.49$ m from the propeller axis in the plane of the propeller. The SPL is calculated in an 11-Hz bandwidth. The propeller with constant angle of attack is predicted to radiate a SPL 4–6 dB lower at low frequencies and about 2-dB lower noise levels at higher frequencies.

VIII. Conclusions

A far-field frequency-domain formulation has been presented for making broadband noise prediction from an open rotor. Predictions of the broadband noise from the R212 propeller are shown to be in reasonable agreement with measured data. The directivities of broadband self-noise are obtained. The predicted feature shows that the main radiation lobe is located along the propeller axis. A preliminary parametric study of the broadband self-noise radiation from propellers with blade tip Mach number, number of blades, chord, blade-setting angle, and angle of attack has been carried out. It shows that a propeller with small chord, large blade number, and constant angle of attack produces lowest noise radiation.

References

[1]Lowson, M. V., "The Sound Field for Singularities in Motion," *Proceedings of the Royal Society, Series A: Mathematical and Physical Sciences*, Vol. 286, No. 1407, 1965, pp. 559–572.

[2]Ffowcs Williams, J. E., and Hawkings, D. L., "Sound Generated by Turbulence and Surfaces in Arbitrary Motion," *Philosophical Transactions of the Royal Society, Series A: Mathematical and Physical Sciences*, Vol. 264, No. 1151, 1969, pp. 321–342.

[3]Farassat, F., "Linear Acoustic Formulas for Calculation of Rotating Blade Noise," *AIAA Journal*, Vol. 19, No. 9, 1981, pp. 1122–1130.

[4]Hanson, D. B., "Helicoidal Surface Theory for Harmonic Noise of Propellers in the Far Field," *AIAA Journal*, Vol. 18, No. 10, 1980, pp. 1213–1220.

[5]Hanson, D. B., "Compressible Helicoidal Surface Theory for Propeller Aerodynamics and Noise," *AIAA Journal*, Vol. 21, No. 6, 1983, pp. 881–889.

[6]Peake, N., and Crighton, D. G., "Lighthill Quadrupole Radiation in Supersonic Propeller Acoustics," *Journal of Fluid Mechanics*, Vol. 223, 1991, pp. 363–382.

[7]Mani, R., "The Radiation of Sound From a Propeller at Angle of Attack," *Proceedings of the Royal Society of London, Series A: Mathematical and Physical Sciences*, Vol. 431, No. 1882, 1990, pp. 203–218.

[8]Hanson, D. B., "Sound From a Propeller at Angle of Attack: A New Theoretical Viewpoint," *Proceedings of the Royal Society of London, Series A: Mathematical and Physical Sciences*, Vol. 449, No. 1936, 1995, pp. 315–328.

[9]Brooks, T. F., "Progress in Rotor Broadband Noise Research," *Vertica*, Vol. 7, No. 4, 1983, pp. 287–307.

[10]Paterson, R. W., and Amiet, R. K., "Nose of a Model Helicopter Rotor due to Ingestion of Isotropic Turbulence," *Journal of Sound and Vibration*, Vol. 85, No. 4, 1982, pp. 551–577.

[11]Amiet, R. K., Simonich, J. C., and Schlinker, R. H., "Rotor Noise Due to Atmospheric Turbulence Ingestion, Part 2: Aeroacoustic Results," *Journal of Aircraft*, Vol. 27, No. 1, 1990, pp. 15–22.

[12]Homicz, G. F., and George, A. R., "Broadband and Discrete Frequency Radiation from Subsonic Rotors," *Journal of Sound and Vibration*, Vol. 36, No. 2, 1974, pp. 151–177.

[13]Howe, M. S., "A Review of the Theory of Trailing Edge Noise," *Journal of Sound and Vibration*, Vol. 61, No. 3, 1978, pp. 437–465.

[14]Roger, M., and Moreau, S., "Back-Scattering Correction and Further Extensions of Amiet's Trailing-Edge Noise Model, Part I: Theory," *Journal of Sound and Vibration*, Vol. 286, No. 3, 2005, pp. 477–506.

[15]Brooks, T. F., and Burley, C. L., "Rotor Broadband Noise Prediction with Comparison to Model Data," AIAA Paper 2001-2210, May 2001.

[16]Zhou, Q., "A Model for Rotor Broadband Noise Prediction," Ph.D. Dissertation, Inst. of Sound and Vibration Research, Univ. of Southampton, Southampton, England, U.K., Oct. 2004.

[17]Corcos, G. M., "Resolution of Pressure in Turbulence," *Journal of the Acoustical Society of America*, Vol. 35, No. 2, 1963, pp. 192–199.

[18]Chou, S. T., and George, A. R., "Effect of Angle of Attack on Rotor Trailing-Edge Noise," *AIAA Journal*, Vol. 22, No. 12, 1984, pp. 1821–1823.

[19]Brooks, T. F., Pope, D. S., and Marcolini, M. A., "Airfoil Self-Noise and Prediction," NASA Reference Publication 1218, 1989, pp. 9–14.

[20]Ffowcs Williams, J. E., and Hall, L. H., "Aerodynamic Sound Generation by Turbulence Flow in the Vicinity of a Scattering Half Plane," *Journal of Fluid Mechanics*, Vol. 40, 1970, pp. 657–670.

[21]Brooks, T. F., and Hodgson, T. H., "Trailing Edge Noise Prediction from Measured Surface Pressures," *Journal of Sound and Vibration*, Vol. 78, No. 1, 1981, pp. 69–117.

[22]Howe, M. S., *Acoustics of Fluid–Structure Interaction*, Cambridge Univ. Press, Cambridge, England, U.K., 1998, Chap. 3.

[23]Yu, J. C., and Joshi, M. C., "On Sound Radiation From the Trailing Edge of a Isolated Airfoil in a Uniform Flow," AIAA Paper 79-0603, March 1979.

[24]Brooks, T. F., and Hodgson, T. H., "Prediction and Comparison of Trailing Edge Noise Using Measured Surface Pressures," AIAA Paper 80-0977, June 1980.

[25]Roger, M., "Trailing Edge Noise Measurements and Prediction for Subsonic Loaded Fan Blades," AIAA Paper 2002-2460, June 2002.

[26]Amiet, R. K., "Effect of the Incident Surface Pressure Field on Noise Due to Turbulence Flow past a Trailing Edge," *Journal of Sound and Vibration*, Vol. 47, No. 3, 1978, pp. 387–393.

[27]Amiet, R. K., "Noise Due to Turbulence Flow past a Trailing Edge," *Journal of Sound and Vibration*, Vol. 47, No. 3, 1976, pp. 387–393.

[28]Howe, M. S., "Trailing Edge Noise at Low Mach Numbers," *Journal of Sound and Vibration*, Vol. 225, No. 2, 1999, pp. 211–238.

[29]Goldstein, M. E., *Aeroacoustics*, McGraw–Hill, New York, 1976.

[30]Metzger, F. B., Magliozzi, B., Towle, G., and Gray, L., "A Study of Propeller Noise Research," *Aerodynamic Noise*, edited by H. S. Ribner, Univ. of Toronto Press, 1969, pp. 371–386.

[31]Hanson, D. B., and Fink, M. R., "The Importance of Quadrupole Sources in Prediction of Transonic Tip Speed Propeller Noise," *Journal of Sound and Vibration*, Vol. 62, No. 1, 1979, pp. 19–38.

[32]Gradshteyn, I. S., and Ryzhik, I. M., *Table of Integrals, Series, and Products* (P710, P979), Academic Press, New York, 1965 (translated from Russian by Scripta Technica, Inc.).

[33]Gutin, L., "On the Sound Field of a Rotating Propeller," *Zhurnal Technicheskoi Fiziki*, Vol 6, 1936, pp. 889–909 (in Russian); translated as NACA TM 1195, 1948.

[34]Trebble, W. J. G., "Investigations of the Aerodynamic Performance and Noise Characteristics of a Dowty Rotol R212 Propeller at Full-Scale in the 24ft Wind Tunnel," *Aeronautical Journal*, Vol. 91, No. 906, 1987, pp. 275–284.